Ragab A. Sayed*[1], Sabry Allam[1], Samia Abdel Fattah[2], Hossam Youssef Hegazy[2], Shadi M. Munshi[3] , M.S. Al-Ashhab[3,4]

J. Electrical Systems 21-1 (2025): 116-136

Regular paper

Designing and modeling a PID control system for energy management in a hybrid electric vehicle powered by photovoltaics, fuel cells, and batteries

Journal of Electrical Systems

This paper presents the development and implementation of a Proportional-Integral-Derivative (PID) control system designed to optimize energy management in a hybrid electric vehicle (HEV). This vehicle integrates multiple power sources, including photovoltaic (solar) panels, fuel cells, and a battery, to enhance overall performance and efficiency. The PID control system effectively manages the energy flow between these sources by dynamically adjusting power distribution based on real-time demands and environmental conditions. Through a series of simulations and real-world tests, the proposed system demonstrates significant improvements in energy utilization, leading to enhanced vehicle performance and reduced reliance on non-renewable energy sources. The results highlight the potential of PID control systems in advancing sustainable transportation technologies by optimizing hybrid powertrain efficiency. Nowadays, vehicle power systems are increasingly turning to renewable and clean energy sources, such as solar power and fuel cells, to address the challenges of global warming. Simulation results from functional tests, including idling, acceleration, and driving under different solar radiation levels and battery states, demonstrate that the proposed power and energy management systems work effectively. Moreover, specific driving cycle test simulations conducted under three scenarios (high, low, and zero solar radiation with different battery states) indicate that the power system operates adaptively under the regulation of the energy management system using PID control.

Keywords: The PID (Proportional-Integral-Derivative) controller, Hybrid Electric Vehicle (HEV), Energy Management Strategy (EMS), Fuel Cells (FCS), and State of Charge (SOC).

1 Introduction

PID controllers have been fundamental to control engineering for over a century due to their simplicity and versatility [1]. However, as industrial processes have evolved into more complex and nonlinear systems, the limitations of traditional PID controllers have become apparent [2]. To address these challenges, advanced variants of PID controllers have been developed, including position PID, incremental PID, differential PID, and fuzzy PID controllers [3]. These innovative designs aim to resolve issues associated with complex, time-varying systems and the difficulties in creating precise mathematical models for such processes [4]. In addition to advancements in PID controller designs, effective correction methods are essential for maintaining optimal system performance despite changing model parameters [5]. The two primary correction approaches are model-based parameter self-tuning and rule-based self-tuning [6]. Model-based methods adjust controller parameters based on mathematical models, while rule-based approaches utilize predefined rules and heuristics for performance optimization [7]. Both strategies aim to enhance the robustness

* Corresponding author: Ragab A. Sayed, Automotive Technology Department, Faculty of Technology and Education, Helwan University, Cairo, Egypt., E-mail: eng.ragab9686@gmail.com

1 Automotive Technology Department, Faculty of Technology and Education, Helwan University, Cairo, Egypt.

2 Electrical Technology Department, Faculty of Technology and Education, Helwan University, Cairo, Egypt.

3 Department of Mechanical Engineering, College of Engineering and Architecture, Umm Al-Qura University, Makkah, Saudi Arabia.

4 Design & Production Engineering Department, Faculty of Engineering, Ain-Shams University, Cairo, Egypt.

and adaptability of PID controllers, ensuring their effectiveness in dynamic industrial environments and unpredictable system dynamics [8]. Overall, while PID controllers remain relevant due to their simplicity and wide applicability, the complexities of modern systems necessitate the development of advanced variants and correction methods to sustain their effectiveness [9].

This paper focuses on modeling and simulating an enhanced PID control system designed to optimize energy management in hybrid electric vehicles powered by fuel cells, solar cells, and batteries. The system has been meticulously calibrated to achieve optimal results in energy management control.

2 PID control theory

The PID (Proportional-Integral-Derivative) controller is a widely used feedback control system in industrial processes and remains the most prevalent control system in process control theory today. This controller considers the present, past, and future values of the error term e(t). With the introduction of digital implementation, modifications to the control system structure have been proposed and adopted in numerous applications. The classical PID controller operates within a feedback control loop and consists of

- The Proportional controller
- The Integral controller
- The Derivative controller

The role of the proportional part depends on the present error, the integral part refers to the accumulation of past mistakes, and the derivative part relates to the prediction of future errors, as illustrated graphically in Fig. 1. The weighted sum of these three components is used for the final adjustment.

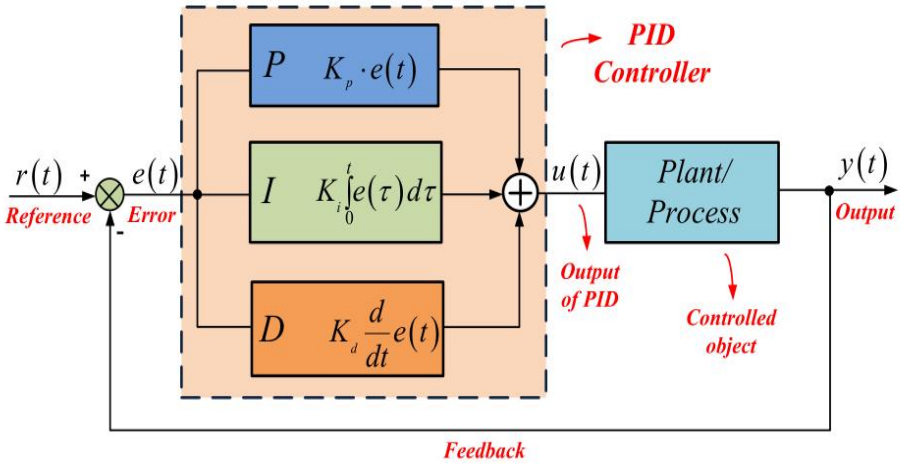

FIGURE 1 Block Diagram of the PID controller employed in a closed-loop system [10].

2.1 Role of the Proportional Controller (P)

Proportional control is a fundamental and widely utilized approach for managing various types of systems. In the context of a proportional controller, the steady-state error exhibits an inverse relationship with the proportional gain; specifically, an increase in gain results in a reduction of the error. The response of the proportional controller can be adjusted by multiplying the error by a constant known as Kp, or proportional gain. The proportional term is given by [10].

$$P = K_p \cdot e(t) \tag{1}$$

Where $e(t) = r(t) - y(t)$ is the error, $r(t)$ is the reference value and $y(t)$ is the output of the closed-loop system of Fig.1.

A high proportional gain (Kp) causes a significant change in the output in response to a given change in error. However, if the proportional gain is excessively high, the system may become unstable. Conversely, a low gain results in a minimal output response, even to a substantial input error. If the proportional gain is too low, the control action may be inadequate for addressing system disturbances. Therefore, proportional gain affects the rise time by reducing it while also decreasing, though not eliminating, the steady-state error. Additionally, it causes a slight change in the settling time. In practice, the Proportional Band (PB) is expressed as a percentage, as shown in [10] Equation 2.

$$PB\% = \frac{100}{K_p} \tag{2}$$

Thus, a PB of 10% corresponds to a gain of K_p=10.

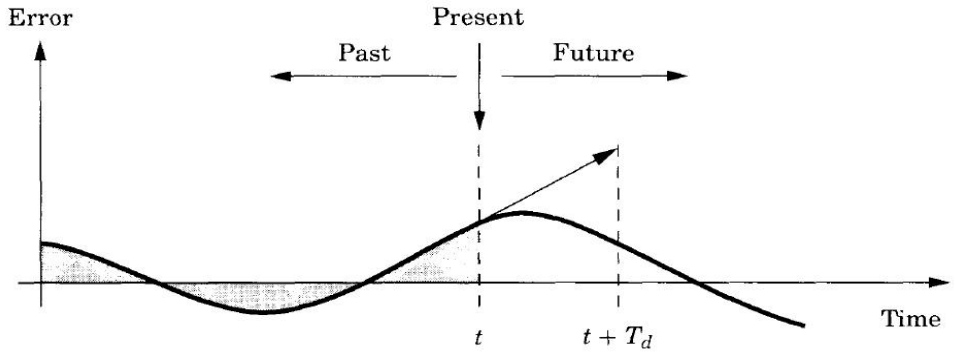

FIGURE 2 The control actions are based on the past, present, and future of the error [11].

2.2 Role of the Integral Controller (I)

An integral controller is directly proportional to both the magnitude and duration of the error. In a PID controller, the integral component represents the cumulative sum of the instantaneous error over time, reflecting the accumulated offset that requires correction. Consequently, increasing the integral gain (Ki) helps eliminate the steady-state error. However, this adjustment may negatively impact the settling time of the transient step response. The integral term is expressed in [10].

$$I = K_i \int_0^t e(\tau) d\tau \tag{3}$$

2.3 Role of the Derivative Controller (D)

The derivative of the process error is determined by calculating the slope of the error over time and multiplying this rate of change by the derivative gain (Kd). This derivative term helps to slow the rate of change of the controller output. Implementing derivative control (D) enhances the stability of the system, reduces overshoot, and shortens the settling time of the transient response. The derivative term is expressed [10].

$$D = K_d \frac{d}{dt} e(t) \tag{4}$$

Effects of each of the controller's parameters K_p, K_d, and K_i on a closed-loop system, with a unit step response depicted in Fig. 3, are summarized in Table 1.

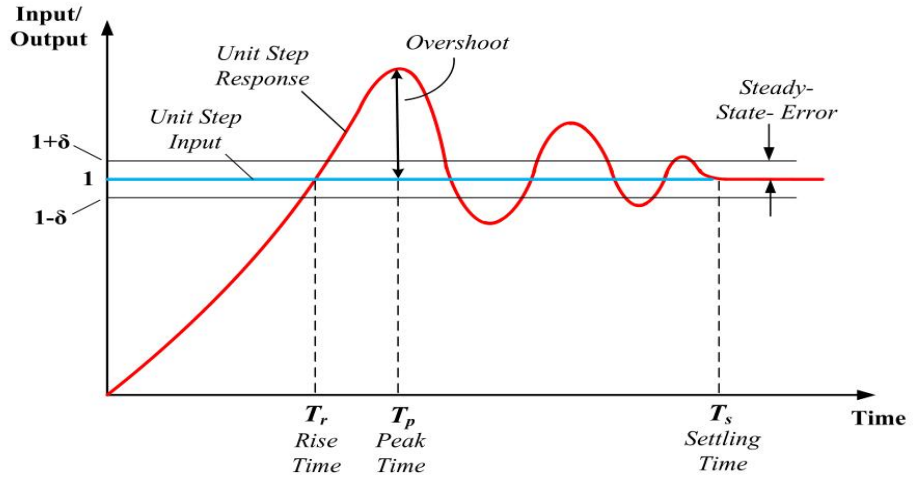

FIGURE 3 Unit step input/response of a closed-loop system [10].

Table 1: Effect of the parameters in the closed-loop system [10].

Parameter Increase	Rise time	Overshoot	Settling time	Steady-state-error
K_p	Decrease	Increase	Small change	Decrease
K_i	Decrease	Increase	Increase	Great reduce
K_d	Small change	Decrease	Decrease	Small change

The time response of the PID controller's output is given by the expression [10].

$$u(t) = K_p \cdot e(t) + K_i \int_0^t e(\tau) d\tau + K_d \frac{d}{dt} e(t) \tag{5}$$

Applying the Laplace transform on the above expression, the transfer function of the PID controller is given by the form [10].

$$C(s) = \frac{U(s)}{E(s)} = K_p + \frac{K_i}{s} + K_d \cdot s \tag{6}$$

$E(s) = L\{e(t)\}$ is the error value and $U(s) = L\{u(t)\}$ is the controller's output, in the frequency domain.

While PID controllers can effectively address many control problems and often deliver satisfactory performance without modifications or tuning, they may underperform in certain applications and generally do not provide optimal control.

3 System Analysis

Figure 4 illustrates the structure of the PVFCHEV system, which comprises a rooftop PV array, a PEMFC stack, a high-pressure hydrogen tank, a lithium battery as a secondary power source, a supervisory controller, and an electric motor with a motor drive. The PV array is connected to a maximum power point tracking (MPPT) converter to ensure maximum output power. Excess solar energy can be stored in the battery when the vehicle is stopped or decelerating. The PEMFC stack serves as the main power source, supplying power to the electric motor. Any excess electricity generated by the fuel cell is used to charge the battery. A flow rate regulator reduces the pressure of the hydrogen flow from the tank and manages its flow rate to adjust the fuel cell's power output.

The lithium-ion battery, known for its high-power density and quick dynamic response, can compensate for transient power demands and absorb excess energy during regenerative braking. A permanent magnet synchronous machine (PMSM) is chosen as the electric motor due to its high operational efficiency and reliability. The supervisory controller monitors the system's status, including the power output of the PV array, the state of charge (SOC) of the battery, and power demand, to determine the fuel cell's power output and the motor's torque.

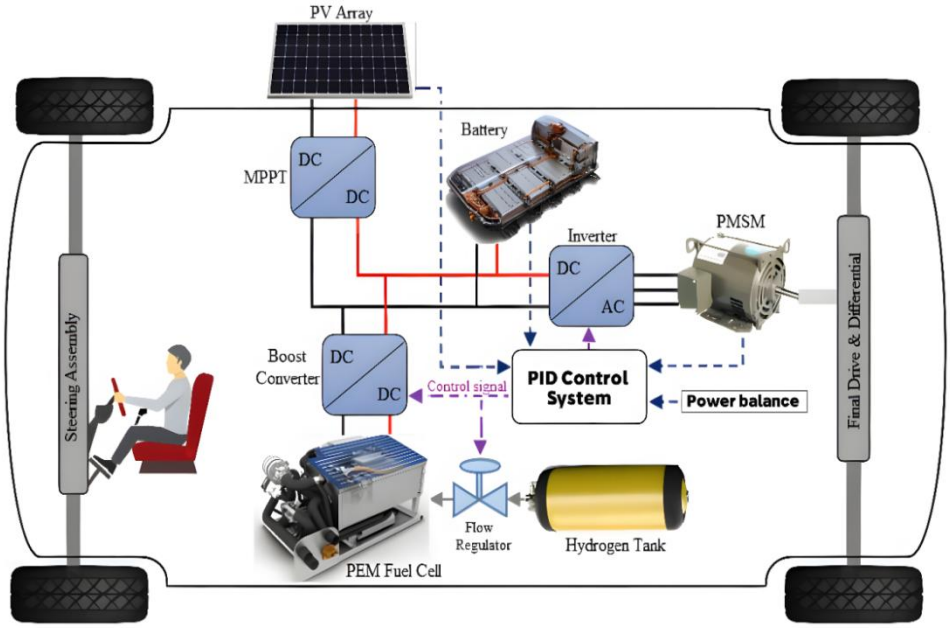

FIGURE 4 The structure of a PV-FC-battery HEV. HEV refers to hybrid electric vehicles; MPPT denotes maximum power point tracking; PEM signifies proton exchange membrane; PMSM represents permanent magnet synchronous machine; and PV-FC indicates photovoltaic-fuel cell.

4 S Y S T E M MODELING

This paper presents the development of a PVFCHEV system model within Matlab/Simulink utilizing the Sim Power Systems package. It establishes a comprehensive physical modeling environment wherein various predefined components are interconnected to facilitate electromechanical systems' modeling, simulation, and analysis [12]. This methodology allows block diagrams to accurately encapsulate the system's architecture,

enabling the automatic generation of system-level equations. Within this research, the PVFCHEV system model is comprised of three primary subsystems: the electrical system, the energy management system, and the vehicle dynamics system.

4.1 Electrical system

The electrical system consists of four primary components: a photovoltaic (PV) array with a maximum power point tracking (MPPT) converter, a lithium-ion (Li-ion) battery, a proton exchange membrane fuel cell (PEMFC) equipped with a boost converter, and a motor. The MPPT converter enhances the low voltage generated by the PV array to the higher voltage required by the direct current (DC) bus while optimizing the power output of the solar panels. The boost converter associated with the PEMFC regulates the fuel cell's output power through current regulation, employing a proportional-integral (PI) control technique. Additionally, the battery connected to the DC bus provides extra power for system startup and assists in recovering the state of charge (SOC) through regenerative braking and surplus energy from the fuel cell. Figure 5 presents the block diagram of the electrical system.

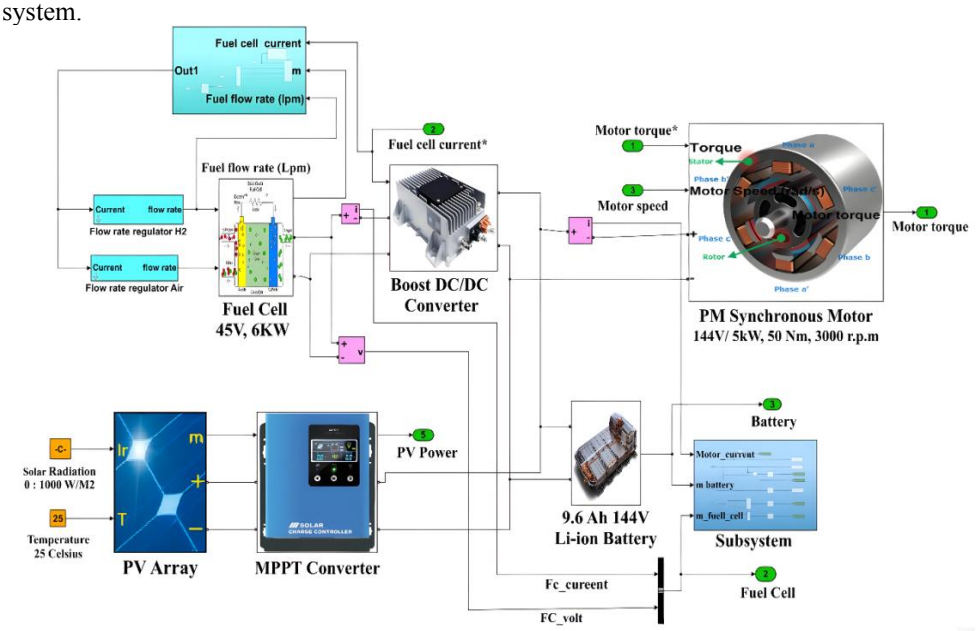

FIGURE 5 The electrical system of a photovoltaic-fuel cell-battery hybrid electric vehicle (PV-FC-battery HEV).

4.1.1 PV array and MPPT converter

The PV array model uses an equivalent circuit embedded within a Simulink PV array block [13]. The following equations present the mathematical models [14]. The solar cell current I is calculated as:

$$I = I_L - I_0 \left[\exp\left(\frac{q(V+IR_S)}{nkT}\right) - 1\right] \quad (7)$$

Where V is the cell voltage, I_o is the diode saturation current, T is the cell temperature (Kelvin), q is the charge of an electron, n is the diode quality factor, and k is Boltzmann's constant. The current source I_L in Equation (8) is defined as:

$$\boldsymbol{I_L = I_{SC}\left(1 + \alpha_t(T - T_{ref})\frac{G}{G_{ref}}\right)} \quad \textbf{(8)}$$

Where G_{ref} is the nominal solar irradiance, assumed to be 1000 W/m²; I_{SC} is the reference nominal short-circuit current under standard conditions; α_t is the temperature coefficient; and T_{ref} is the temperature for standard conditions, set at 25°C. The diode saturation current I_O is defined as:

$$\boldsymbol{I_0 = I_{0(ref)}\left[\left(\frac{T}{T_{ref}}\right)^3 \exp\left(\frac{-qE_g}{nk}\left(\frac{1}{T} - \frac{1}{T_{ref}}\right)\right)\right]} \quad \textbf{(9)}$$

Where E_g is the bandgap voltage and $I_{0(ref)}$ is the saturation current under standard conditions. The MPPT converter continuously adjusts the operating point of the PV panel to ensure it operates at the maximum power point for the given irradiation and temperature. The converter employs the Perturb and Observe (P&O) algorithm-based MPPT technique [15]. The roof area of a typical lightweight vehicle is approximately 2 m², allowing for the installation of up to a 500 W PV array. The specifications of the PV array for the 6 kW class lightweight PVFCHEV studied here are detailed in Table 2.

Table 2: The specifications of the PV array

Parameter	Value	Unit
Series-connected modules	2	Piece
Cells per module	72	Piece
Maximum current at MPP	5.84	A
Maximum voltage at MPP	42.8	V
Short circuit current (I_{sc})	6.2	A
Open circuit voltage (V_{oc})	50.93	V
Maximum power per module	250	W

Abbreviation: PV, photovoltaic.

4.1.2 Fuel Cell and Boost Converter

The model of the PEMFC stack is based on the detailed fuel cell stack model provided in Simulink [16]. The mathematical representation of the PEMFC is presented in the following equations [17].
The voltage of the fuel cell stack V_{FC} is:

$$\boldsymbol{V_{FC} = E_{OC} - NA\ln\left(\frac{i_{FC}}{i_0}\right)\frac{1}{\frac{sT_d}{3}+1} - Ri_{FC}} \quad \textbf{(10)}$$

Where E_{OC} is the open circuit voltage, i_{FC} is the current of the FC stack, A is the Tafel slope, it is the exchange current, N is the number of cells, T_d is the reaction time, and R is the internal resistance. The open circuit voltage E_{OC} is:

$$\boldsymbol{E_{OC} = K_C E_n} \quad \textbf{(11)}$$

Where K_C is the voltage constant under nominal operating conditions, and E_n is the Nernst voltage. The exchange current i_o is calculated as:

$$\boldsymbol{i_0 = \frac{zFk\left(P_{H_2}+P_{O_2}\right)}{Rh} e^{\frac{-\Delta G}{RT}}} \quad \textbf{(12)}$$

Where z represents the number of moving electrons, F is Faraday's constant, k is Boltzmann's constant, R is the ideal gas constant, h is Planck's constant, T is the cell temperature in Kelvin (K), ΔG is the size of the activation barrier, P_{H2} is the partial pressure of hydrogen, and P_{O2} is the partial pressure of oxygen inside the stack in atmospheres (atm). The Tafel slope A is shown as:

$$\boldsymbol{A = \frac{RT}{z\alpha F}} \quad \textbf{(13)}$$

Where α is the charge transfer coefficient. The partial pressure of hydrogen and oxygen are expressed as:

$$\boldsymbol{P_{H_2} = \left(1 - U_{fH_2}\right)x\,\%P_{fuel}} \quad \textbf{(14)}$$

$$\boldsymbol{P_{fO_2} = \left(1 - U_{fO_2}\right)y\,\%P_{air}} \quad \textbf{(15)}$$

Where P_{fuel} is the fuel pressure, U_{fH2}(%) is the nominal utilization rate of hydrogen, x% is the percentage of hydrogen in the fuel, P_{air} is the air pressure, U_{fO2}(%) is the nominal utilization rate of oxygen, and y% is the percentage of oxygen. The utilization rates of hydrogen and oxygen are calculated as follows:

$$\boldsymbol{U_{fH_2} = \frac{6000RTNi_{FC}}{zFP_{fuel}V_{fuel}x\%}} \quad \textbf{(16)}$$

$$\boldsymbol{U_{fH_2} = \frac{6000RTNi_{FC}}{2zFP_{air}V_{air}y\%}} \quad \textbf{(17)}$$

Where, V_{fuel} (L/min) indicates the flow rate of hydrogen fuel, while V_{air} signifies the airflow rate.

The DC-DC converter for the fuel cell (FC) employs a boost-type configuration, and a proportional-integral (PI) controller manages the FC's power by tracking the reference current (i_{FC}) set by the PID controller [18]. Figure 6 depicts the control scheme of the converter, and Table 3 provides detailed specifications of the FC based on the parameters from the embedded Simulink model.

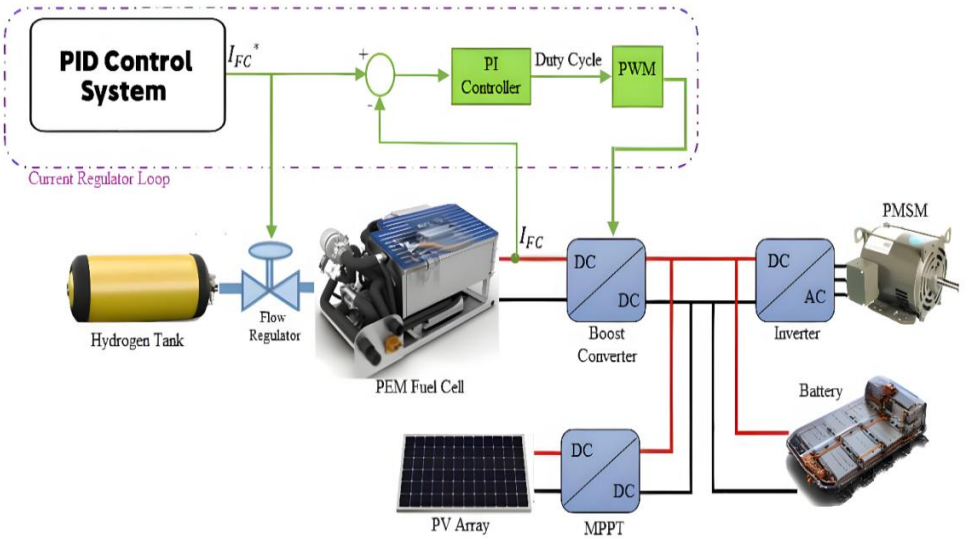

FIGURE 6 The PID control strategy for the fuel cell boost converter includes maximum power point tracking (MPPT), proton exchange membrane (PEM) technology, and the utilization of a permanent magnet synchronous machine (PMSM).

Table 3: **The specifications of PEMFC**

Parameter	Value	Unit
Number of cells	65	Piece
Nominal voltage	45	V
Nominal power	4.2	KW
Peak power	6	KW
Fuel supply pressure	1.5	bar
Operating temperature	65	°C
Nominal stack efficiency	55	%

4.1.3 Battery and Electric Motor

A Li-ion battery pack is utilized, with its dynamic model detailed in Reference [19]. For the lightweight electric vehicle (EV), the DC bus voltage is set at 144 V, which is lower than that of conventional EVs due to considerations of safety, cost, and technical performance. The Li-ion battery pack comprises twelve series-connected modules, each providing 12 V and 0.8 Ah, resulting in a total capacity of 144 V and 9.6 Ah.

The electric motor is a 144 V, 5 kW interior permanent magnet synchronous motor (PMSM), paired with a driver based on the PM Synchronous Motor Drive (AC6) block available in Simulink [20]. This motor drive incorporates a closed-loop speed control system using the vector control method [21]. **In this research, the PMSM's maximum torque is specified as 50 Nm, and its maximum motor speed is 3000 rpm.**

4.2 Energy management system

The energy management system generates reference signals for both the motor drive and the DC/DC converter of the fuel cell, enabling effective power distribution among various electric sources.

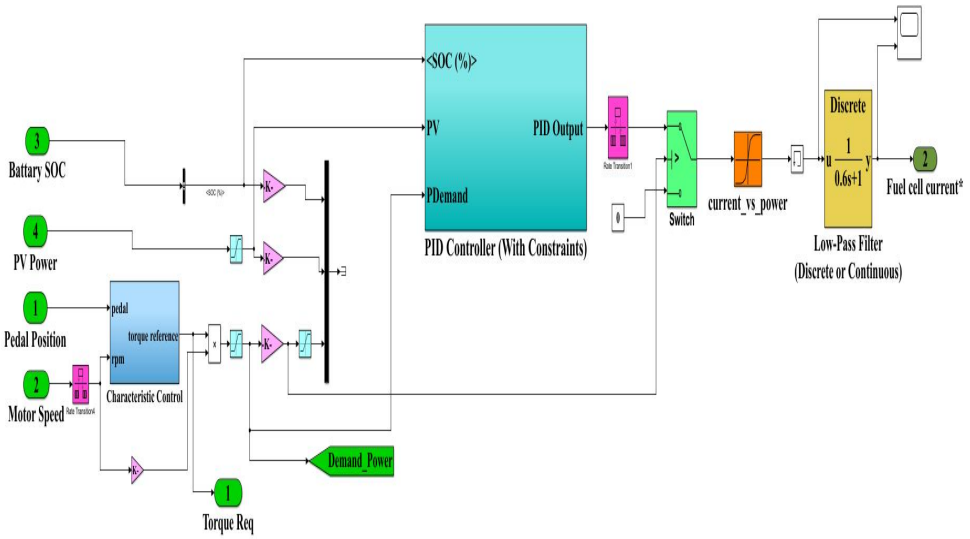

FIGURE 7 The block diagram of the energy management system.

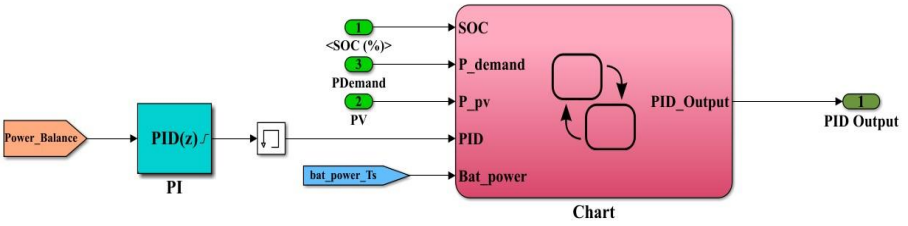

FIGURE 8 The block diagram of the inputs and outputs of a PID control system.

Figure 8 presents the system's block diagram, which processes four input signals: battery state of charge (SOC), photovoltaic (PV) power, pedal position, and motor speed. The pedal position signal is produced by the Longitudinal Driver block within Simulink, which uses a PID controller to generate normalized pedal signals that align with the speed profile of a specified driving cycle [22]. Power demand is calculated by multiplying the required motor torque by the motor speed.

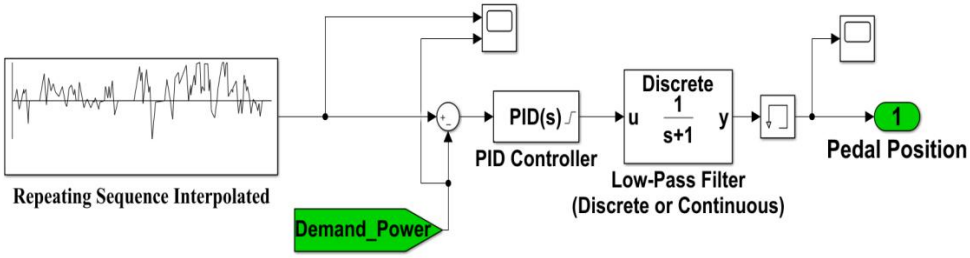

FIGURE 9 The block diagram of the pedal position signal generation.

The input parameters for PV power (P_{PV}) and driving power demand (P_{demand}) are scaled to a range of 0 to 1 using the following equations:

$$\boldsymbol{\theta(P_{PV})} = \frac{\boldsymbol{P_{PV}}}{\boldsymbol{P_{PV}^{max}}} \tag{18}$$

$$\boldsymbol{\theta(P_{demand})} = \frac{\boldsymbol{P_{demand}}}{\boldsymbol{P_{demand}^{max}}} \tag{19}$$

Where P_{PV}^{max} and $P_{\text{demand}}^{\max}$ Represent the maximum power of the PV array and the peak power of the motor, respectively. The PID controller employs the control strategy outlined in Section 4.2. By inputting the parameters of power balance, battery state of charge (SOC), solar power, and motor power demand, the controller generates the parameter $\theta(P_{FC})$, which is then used as the reference power for the fuel cell (FC) as follows:

$$\boldsymbol{P_{FC}} = \boldsymbol{\alpha\theta(P_{FC})} \tag{20}$$

Where α is the proportional gain and P_{FC} is the reference power of the fuel cell (FC). The reference power is converted into the reference current using the polarization curve of the FC. The lifespan of the FC can be significantly reduced if its operating conditions undergo frequent and drastic changes. To mitigate the degradation of the FC, a rate limiter restricts the rate of change of FC power to within 0.5 kW/s. It is important to note that, in this study, the power range for operating the FC system is between 0.6 and 6 kW, with the motor's peak power at 5 kW and the maximum power of the photovoltaic (PV) array at 0.5 kW.

4.3 Vehicle dynamics

The vehicle dynamics system models the mechanical transmission components of the Vehicle [23], as shown in Figure 10. This model focuses exclusively on regenerative braking, emphasizing the performance of both the electrical system and the energy management system (EMS) [24]. For this analysis, road inclination and wind speed are set to zero. Vehicle specifications can be found in Table 4 [25].

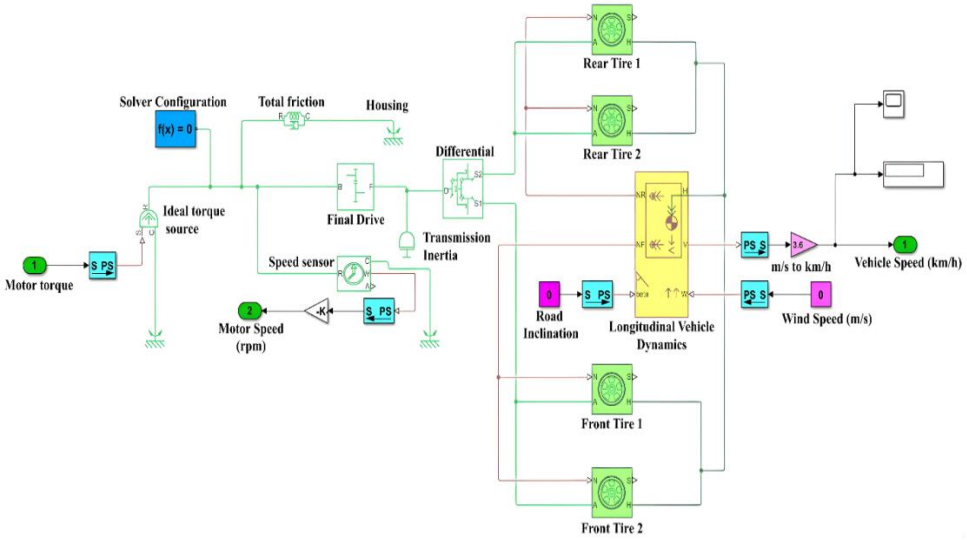

FIGURE 10 The block diagram of the vehicle dynamics system

Table 4: The main parameters of the PVFCHEV

Parameter	Value	Unit
Total mass	800	kg
Maximum speed	60	km/h
Frontal area	2.3	m^2
Rolling radius of the tires	0.2	m
Wheelbase	2.5	m
Gear ratio of the final drive	3.0	-
Aerodynamic drag coefficient	0.36	-

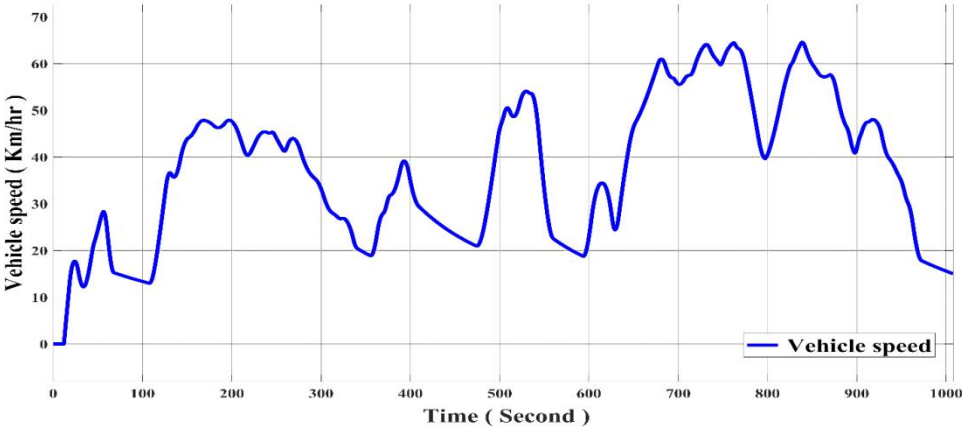

FIGURE 11 The vehicle speed curve duration driving cycle

5 SIMULATION RESULTS AND DISCUSSIONS

5.1 Functional test results

The functional test simulates the operation of the PV-FC-battery HEV across various modes during a driving cycle, including idling, starting, cruising, accelerating, and regenerative braking. The testing procedure is as follows:

1. t = 0 – 2 seconds: The vehicle is stopped, and the PV array charges the battery.
2. t = 2 – 6 seconds: The pedal position is set to 70% (starting).
3. t = 6 – 11 seconds: The pedal is released to 25% (cruising).
4. t = 11 – 16 seconds: The pedal is pushed to 85% (accelerating).
5. t = 16 seconds: The pedal position is set to -70% (regenerative braking).

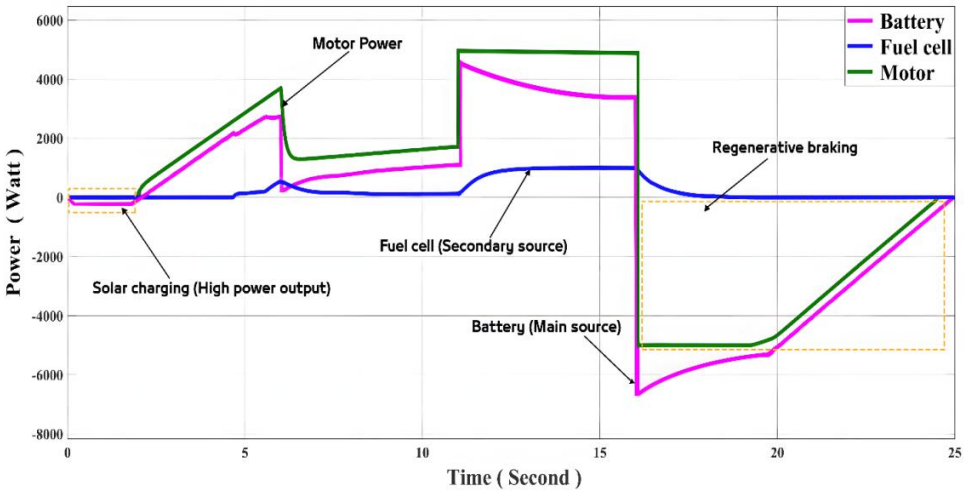

FIGURE 12 The power flow of the PVFCHEV system in the functional test.

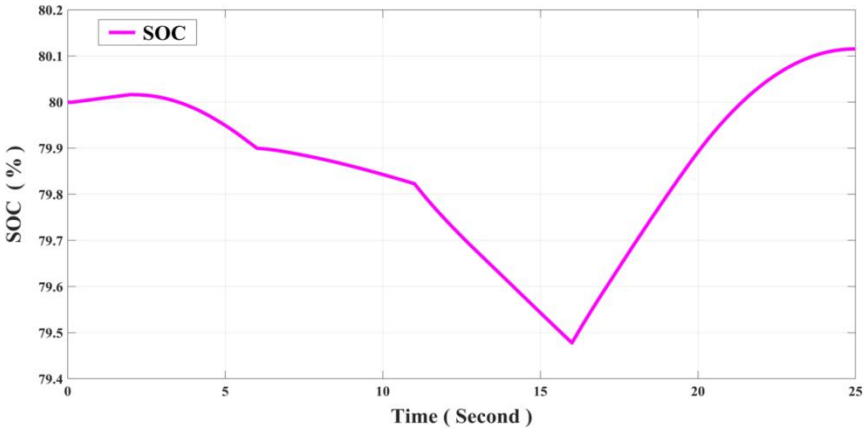

FIGURE 13 The battery state of charge (SOC) of the PVFCHEV system in the functional test.

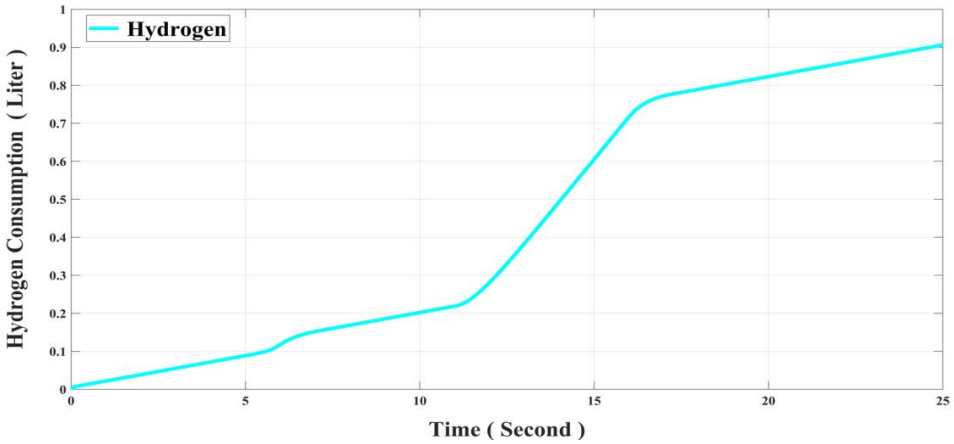

FIGURE 14 The hydrogen consumption of the PVFCHEV system in the functional test.

Figures 12, 13, and 14 show the simulation results under conditions where solar radiance is 1000 W/m², the ambient temperature is 25°C, and the initial battery state of charge (SOC) is 80%.

Due to intense solar radiation and the high state of charge (SOC) of the battery, the battery serves as the primary power source. As shown in Figure 12, when the vehicle comes to a stop, the battery displays a negative power value, indicating that it is being charged by solar energy.

During acceleration, the battery and the photovoltaic (PV) array work together to power the vehicle until the fuel cell (FC) activates to meet the increased power demand. When power demand decreases, the battery absorbs excess power from the FC, which cannot immediately reduce its output. At peak power, the battery remains the main power source, while the FC acts as a secondary source, helping to lower the battery's SOC to a more manageable level.

When the driver applies the brakes, the battery captures kinetic energy through regenerative braking, while the PV array continues to charge the battery. Figure 15 illustrates the performance of the PVFCHEV under varying solar radiation levels and battery states.

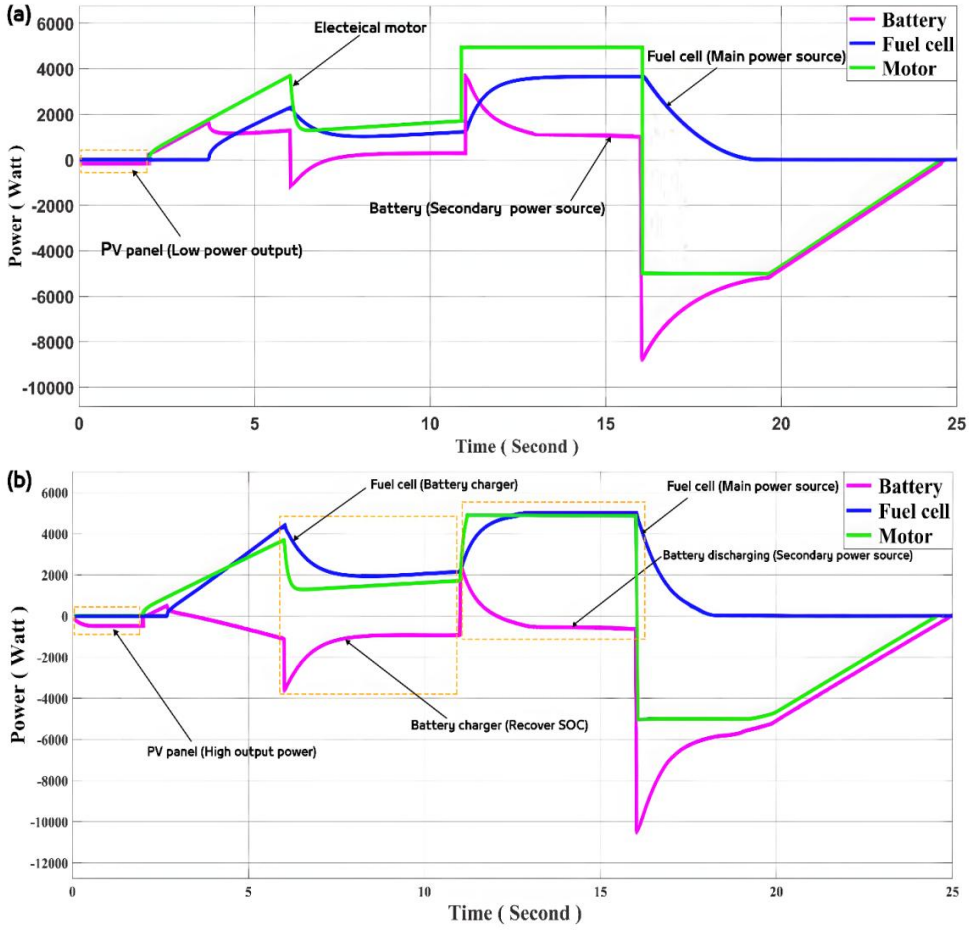

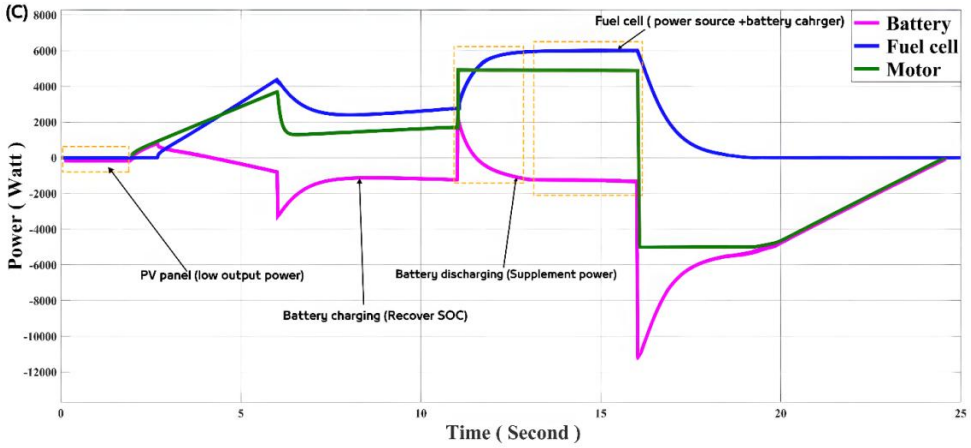

FIGURE 15 The performance of the PVFCHEV under different situations: A, Solar radiance = 400 W/m^2, initial battery SOC = 80%; B, Solar radiance = 1000 W/m^2, initial battery SOC = 30%; C, Solar radiance = 400 W/m^2, initial battery SOC = 30%. PVFCHEV, photovoltaic-fuel cell-battery hybrid electric vehicle; SOC, state-of-charge

In Figure 15A, solar radiation is weak, and the battery's state of charge (SOC) is high. As a result, the battery operates as a secondary power source, supplying a small portion of the driving power.

In Figure 15B, abundant solar power coincides with a low battery SOC. In this scenario, the fuel cell (FC) acts as the primary power source, quickly charging the battery to restore its SOC. Due to the strong solar radiation, it is crucial to reserve some battery capacity for storing solar energy. Consequently, when the motor demands peak power, the battery contributes a small amount, allowing the FC to operate with relatively high efficiency.

In Figure 15C, to avoid potential damage from over-discharging the battery, the FC generates extra power when both the battery SOC and solar power are low. The battery only discharges to offset any power deficit during vehicle acceleration.

Figures 12, 13, 14, and 15 demonstrate that the electrical system of the photovoltaic fuel cell hybrid electric vehicle effectively performs its key functions, including vehicle propulsion, power distribution regulation, and electric motor control. The energy management system (EMS) exhibits strong performance, even in the face of variations in solar radiation, battery status, and driving conditions.

5.2 Driving cycle test results

The World Harmonized Light-duty Test Procedures (WLTP) Class 1 driving cycle [26] serves as the standard for evaluating the performance of lightweight PVFCHEVs as shown in Figure (16) and Table (5). To simulate various environmental conditions and battery states.

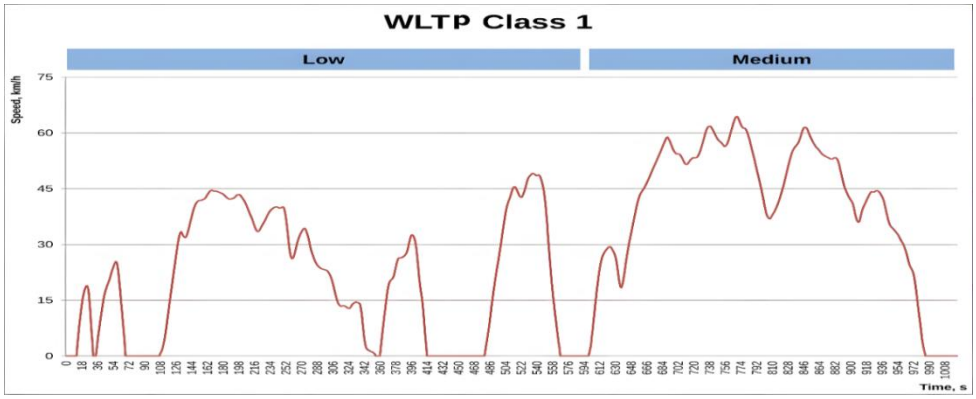

FIGURE 16 The World Harmonized Light-duty Test Procedures Class 1 driving cycle

TABLE 5 The main parameters of The WLTP Class 1 driving cycle

Parameter	Low	Medium	Total
Duration, S	589	433	1022
Stop duration, S	155	48	203
Distance, m	3324	4767	8091
% of stops	26.3 %	11.1 %	19.9 %
Maximum speed, Km/hr	49.1	64.4	
Average speed without stops, Km/hr	27.6	44.6	35.6
Average speed with stops, Km/hr	20.3	39.6	28.5
Minimum acceleration, m/s^2	-1	-0.6	
Maximum acceleration, m/s^2	0.8	0.6	

Abbreviation: WLTP, The World Harmonized Light-duty Test Procedures.

We have established three distinct scenarios, which are detailed in the following sections.
Scenario 1: Under sunny conditions, with solar radiation measured at 1000 W/m², the photovoltaic (PV) array effectively charges the battery, increasing the initial state of charge is 80%.

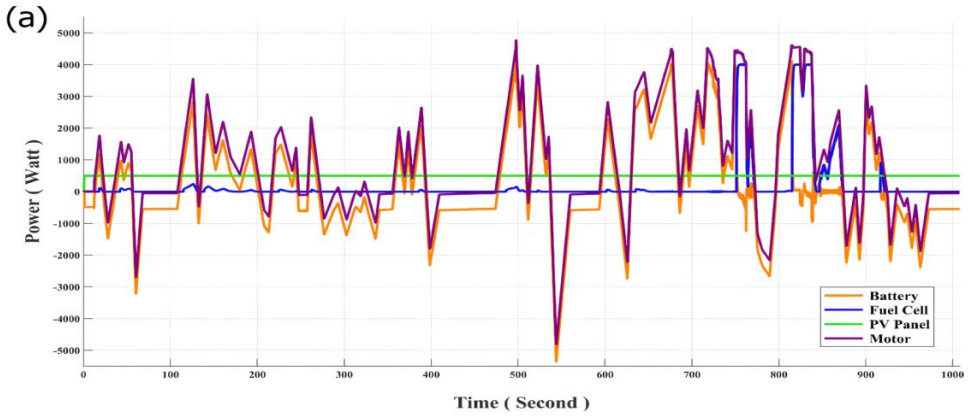

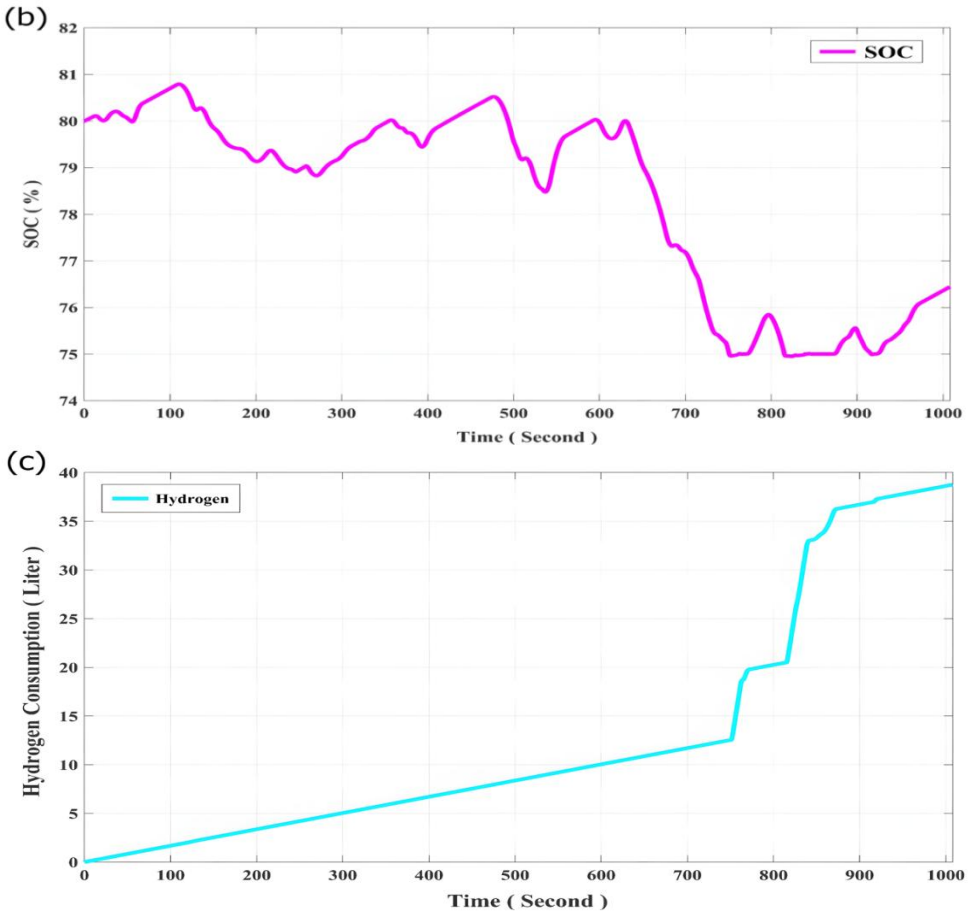

FIGURE 17 The performance of the PVFCHEV in Scenario 1: A, Power curves; B, Battery SOC curve. C, Hydrogen consumption curve, PVFCHEV, photovoltaic-fuel cell-battery hybrid electric vehicle; SOC, state-of-charge

Figure 17 illustrates the power distribution of the PV-FC-HEV (photovoltaic-fuel cell hybrid electric vehicle) power system, as well as the battery SOC for Scenario 1. In Figure 17A, the output power of the PV array is substantial, allowing the battery to serve as the primary power source according to the energy management system (EMS). The FC operates in a low power range, where its efficiency is relatively high, and remains inactive when power demand is minimal. The battery is programmed to discharge its stored energy to maximize solar energy capture; as a result, the battery SOC generally decreases, as shown in Figure 17B.
Figure17 C shows the rate of hydrogen fuel consumption during this condition.

Scenario 2: In contrast, during overcast and rainy conditions, where solar radiation drops to 400 W/m², the power generated by the PV array is insufficient due to the reduced solar intensity, leading to an initial SOC of 30%.

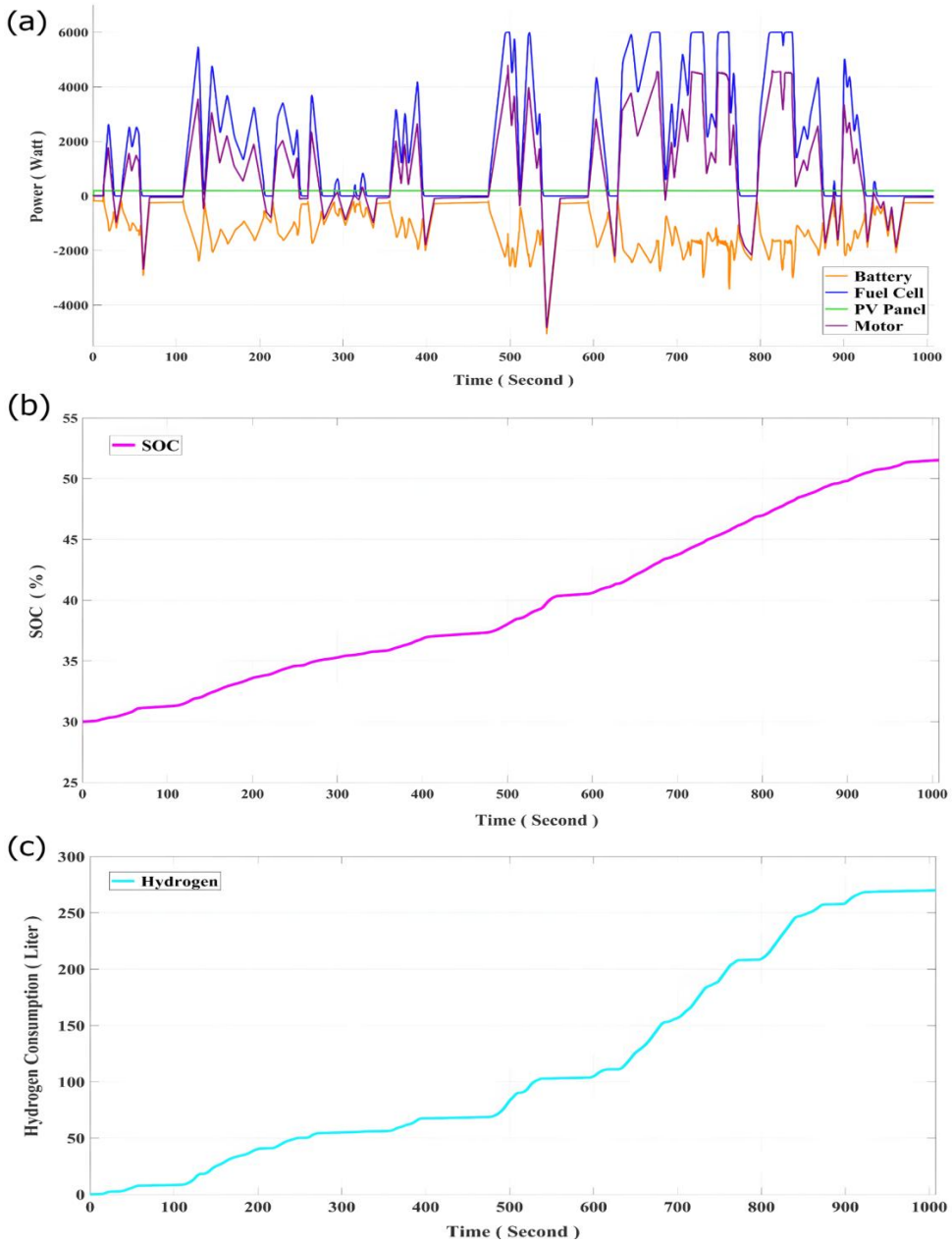

FIGURE 18 The performance of the PVFCHEV in Scenario 1: A, Power curves; B, Battery SOC curve. C, Hydrogen consumption curve, PVFCHEV, photovoltaic-fuel cell-battery hybrid electric vehicle; SOC, state-of-charge

Figure 18 illustrates the power curves of the system and the battery state of charge (SOC) in Scenario 2. Initially, the fuel cell (FC) generates more power than the demand, aiming to raise the battery SOC to a mid-level. Once the battery SOC reaches approximately 40%, the FC reduces its excessive power generation and begins to match the power demand,

allowing the battery to provide supplemental power for acceleration as shown in Figure (18).

Scenario 3: At night, when solar radiation falls to 0 W/m², the PV array becomes inactive. Consequently, the power supplied to the vehicle comes solely from the fuel cell (FC) and the battery, which starts with an initial SOC of 50%.

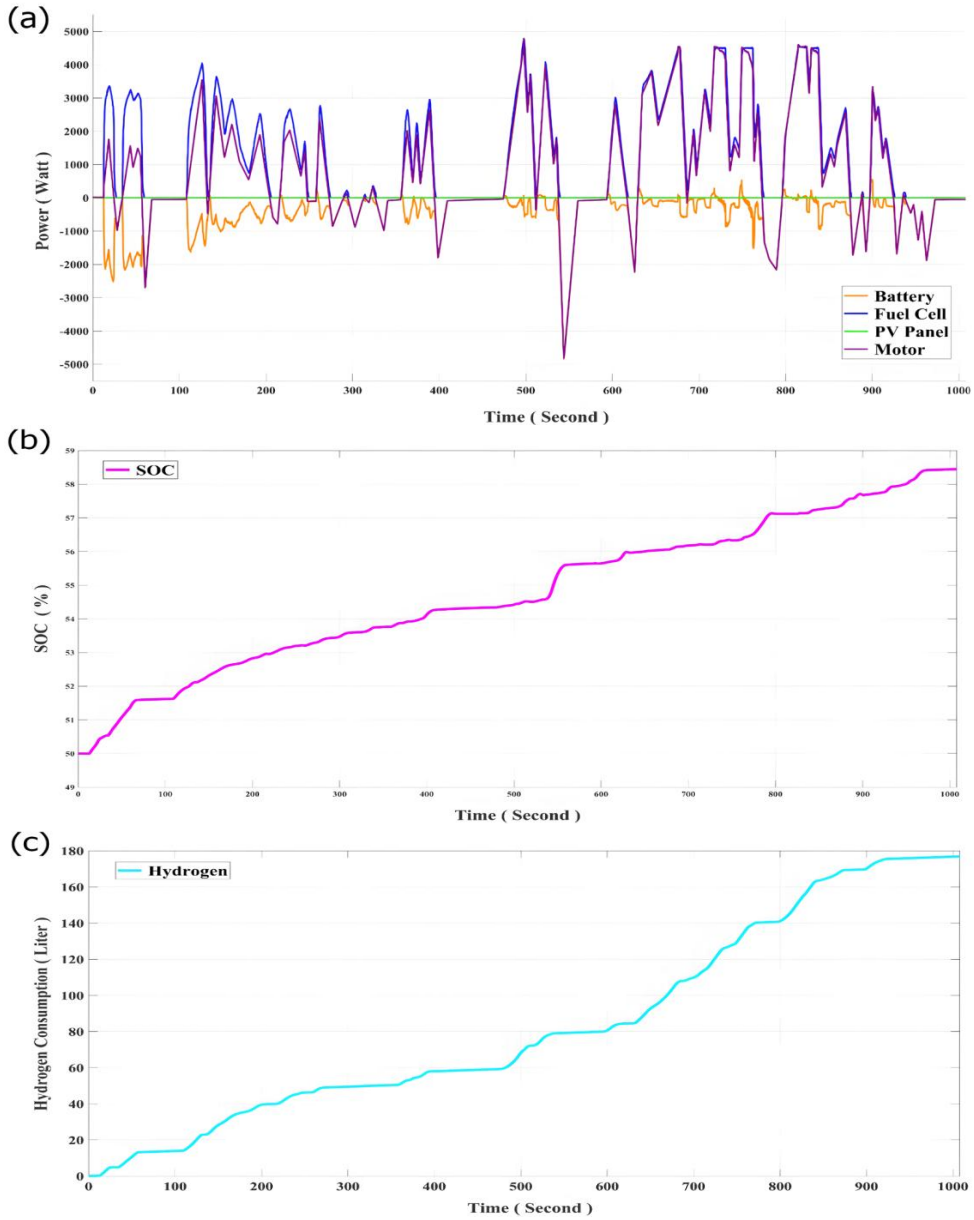

FIGURE 19 The performance of the PVFCHEV in Scenario 1: A, Power curves; B, Battery SOC curve. C, Hydrogen consumption curve, PVFCHEV, photovoltaic-fuel cell-battery hybrid electric vehicle; SOC, state-of-charge

In the night scenario, when the photovoltaic (PV) array is offline and only the fuel cells and battery are operational, a PID control power management strategy regulates the fuel cell

output power in response to changes in thrust and makes it the primary power source, with the battery acting as a temporary power source as shown in Figure (19).

6 CONCLUSIONS

The paper investigates the technical feasibility of a hybrid electric vehicle (HEV) integrating photovoltaic panels, fuel cells, and batteries through a model-based approach and an energy management strategy. A 6 kW PV-FC-HEV system is modeled using MATLAB/Simulink, which incorporates electrical systems, an energy management system (EMS), and vehicle dynamics. The EMS employs a PID control strategy that takes inputs such as power balance, demand power, photovoltaic array output, and battery state of charge (SOC) to determine the reference power for the fuel cell. The aim is to optimize power distribution and maximize the use of solar energy despite its intermittency. Simulations validate the model and EMS through functional and driving cycle tests, demonstrating successful vehicle propulsion and effective power distribution regulation. The feasibility of the PV-FC-HEV is confirmed under varying solar radiation and battery conditions. During a WLTP driving cycle test, the EMS efficiently manages rapid changes in power demand and variations in solar energy, The study's modeling and simulations establish a foundation for future research, emphasizing the need for experimental validation. Future work should focus on experiments to validate the PV-FC-HEV and its EMS, supported by the developed physical model for experimental setups.

REFERENCES

[1] Y. Wei, “Analysis And Optimization of Automotive Systems Based on PID Control,” *Highlights Sci. Eng. Technol.*, vol. 71, pp. 11–17, Nov. 2023, doi: 10.54097/hset.v71i.12371.

[2] S. Bennett, “Development of the PID Controller,” *Control Syst. IEEE*, vol. 13, pp. 58–62, Jan. 1994, doi: 10.1109/37.248006.

[3] V. Kumar, B. C. N. Nakra, and A. Mittal, “A Review of Classical and Fuzzy PID Controllers,” *Int. J. Intell. Control Syst.*, vol. 16, pp. 170–181, Sep. 2011.

[4] L. O. Tedeschi, “Review: The prevailing mathematical modeling classifications and paradigms to support the advancement of sustainable animal production,” *animal*, vol. 17, p. 100813, 2023, doi: https://doi.org/10.1016/j.animal.2023.100813.

[5] P. Veysi, M. Adeli, and N. Naziri, *Introduction to PID Controller and Model Predictive Control in Engineering Systems*. 2024.

[6] K. Kim, P. Rao, and J. Burnworth, “Self-Tuning of the PID Controller for a Digital Excitation Control System,” *Ind. Appl. IEEE Trans.*, vol. 46, pp. 1518–1524, Sep. 2010, doi: 10.1109/TIA.2010.2049631.

[7] H. Rizk, A. Chaibet, and A. Kribèche, “Model-Based Control and Model-Free Control Techniques for Autonomous Vehicles: A Technical Survey,” *Appl. Sci.*, vol. 13, p. 6700, May 2023, doi: 10.3390/app13116700.

[8] N. Ajlouni, “Enhancing PID Control Robustness in CSTRs Through a Hybrid Approach to Tuning Under External Disturbances with GA, PSO, and Machine Learning,” Sep. 2024, doi: 10.21203/rs.3.rs-5150659/v1.

[9] K. Ang, G. Chong, and Y. Li, “PID Control System Analysis, Design, and Technology,” *Control Syst. Technol. IEEE Trans.*, vol. 13, pp. 559–576, Aug. 2005, doi: 10.1109/TCST.2005.847331.

[10] I. Dimeas, “Design of integrated fractional-order controllers,” , Master thesis, 2017.

[11] S. Dormido, “Advanced PID Control - [Book Review],” *Control Syst. Mag. IEEE*, vol. 26, pp. 98–101, Mar. 2006, doi: 10.1109/MCS.2006.1580160.

[12] M. Al-Dhaifallah, M. M. Refaat, Z. Alaas, S. H. E. Abdel Aleem, and Z. M. Ali, “Enhancing hosting capacity for electric vehicles in modern power networks using improved hybrid optimization approaches with environmental sustainability considerations,” *Sci. Rep.*, vol. 14, no. 1, p. 25607, 2024.

[13] M. Nfaoui *et al.*, "Comprehensive modeling and simulation of photovoltaic system performance by using matlab/simulink: integrating dynamic meteorological parameters for enhanced accuracy," *J. Umm Al-Qura Univ. Appl. Sci.*, pp. 1–24, 2024.

[14] N. J. Mlazi, M. Mayengo, G. Lyakurwa, and B. Kichonge, "Mathematical modeling and extraction of parameters of solar photovoltaic module based on modified Newton–Raphson method," *Results Phys.*, vol. 57, p. 107364, 2024, doi: https://doi.org/10.1016/j.rinp.2024.107364.

[15] Y. Lozanov and S. Tzvetkova, "Model-comparative Analysis of MPPT Algorithms for Control of DC/DC Converters Used in PV Systems," in *2024 16th Electrical Engineering Faculty Conference (BulEF)*, 2024, pp. 1–5. doi: 10.1109/BulEF63204.2024.10794882.

[16] S. Beni Hamed and M. Ben Hamed, "Modeling and Simulation of a Proton Exchange Membrane Fuel Cell Stacks in MATLAB/SIMULINK Under Conditions Variations," in *International Conference on Green Energy Conversion System*, Springer, 2023, pp. 255–266.

[17] S. Kar, C. K. Chanda, and S. Banerjee, "Mathematical modelling and performance study of proton exchange membrane fuel cell," in *2024 International Conference on Advances in Modern Age Technologies for Health and Engineering Science (AMATHE)*, IEEE, 2024, pp. 1–5.

[18] S. Somkun, C. Sirisamphanwong, and S. Sukchai, "A DSP-based interleaved boost DC–DC converter for fuel cell applications," *Int. J. Hydrogen Energy*, vol. 40, no. 19, pp. 6391–6404, 2015, doi: https://doi.org/10.1016/j.ijhydene.2015.03.069.

[19] C. Fan, K. Liu, Y. Ren, and Q. Peng, "Characterization and identification towards dynamic-based electrical modeling of lithium-ion batteries," *J. Energy Chem.*, vol. 92, pp. 738–758, 2024, doi: https://doi.org/10.1016/j.jechem.2024.01.040.

[20] S. A. Agoro, *Design Modeling and Predictive Control of Dual Three Phase Permanent Magnet Synchronous Motors for Traction Applications*. North Carolina State University, 2023.

[21] M. Monadi, M. Nabipour, F. Akbari-Behbahani, and E. Pouresmaeil, "Speed Control Techniques for Permanent Magnet Synchronous Motors in Electric Vehicle Applications Toward Sustainable Energy Mobility: A Review," *IEEE Access*, vol. 12, pp. 119615–119632, 2024, doi: 10.1109/ACCESS.2024.3450199.

[22] O. S. Showers, "Development of an energy management system for fuel cell/lithium-ion battery hybrid electric vehicles." Cape Peninsula University of Technology, 2022.

[23] B. K. Powell, K. E. Bailey, and S. R. Cikanek, "Dynamic modeling and control of hybrid electric vehicle powertrain systems," *IEEE Control Syst. Mag.*, vol. 18, no. 5, pp. 17–33, 1998, doi: 10.1109/37.722250.

[24] M. S. Munsi and H. Chaoui, "Energy Management Systems for Electric Vehicles: A Comprehensive Review of Technologies and Trends," *IEEE Access*, 2024.

[25] J. J. Hwang, D. Y. Wang, and N. C. Shih, "Development of a lightweight fuel cell vehicle," *J. Power Sources*, vol. 141, no. 1, pp. 108–115, 2005, doi: https://doi.org/10.1016/j.jpowsour.2004.08.056.

[26] S. Feng and R. Qu, "Efficiency Estimates of Integrated Two-Speed e-Powertrain System under WLTP Driving Cycle for Electric Vehicle," in *2023 26th International Conference on Electrical Machines and Systems (ICEMS)*, IEEE, 2023, pp. 35–40.